



Study on the effect of rivet die parameters on joint quality of self-piercing riveting employed 3D modeling and MCDM method

Dengfeng Wang¹ · Dewen Kong¹ · Chong Xie¹ · Shenhua Li¹ · Ling Zong¹

Received: 25 June 2021 / Accepted: 15 January 2022 / Published online: 27 January 2022
© The Author(s), under exclusive licence to Springer-Verlag London Ltd., part of Springer Nature 2022

Abstract

Self-piercing riveting (SPR) as a new type of dissimilar material joining technology has been widely used in the field of automobile manufacturing. In this paper, the smooth particle Galerkin (SPG) algorithm was used to establish the SPR 3D finite element model connecting steel and aluminum sheets to simulate the forming and cross-tension of the joint, and the accuracy of the simulation was verified by experiment. The effects of rivet length, rivet blade angle, rivet shank thickness, die diameter, and die depth on the cross-sectional dimensions and cross-tension strength of the joint were studied. The technique for order preferences by similarity to ideal solution (TOPSIS) combined with entropy method was proposed to solve the current problem, which is the difficulty to select a combination of rivet and die that can obtain the best joint quality objectively and accurately. The results showed that the best joint quality can be obtained when a combination of rivet and die with rivet length of 6.5 mm, rivet blade angle of 50°, rivet shank thickness of 1.2 mm, die diameter of 10 mm, and die depth of 1.7 mm was selected. In comparison with the benchmark combination, this combination increased by 90.9% in undercut, reduced by 44.7% in the remaining thickness of the bottom, increased by 16.2% in rivet shank flaring, and increased by 2.5% in cross-tension strength. This research provides references for the model selection and size design of rivets and dies.

Keywords Self-piercing riveting (SPR) · Smoothed Particle Galerkin (SPG) · Joint quality · Entropy method · TOPSIS method

1 Introduction

With the continuous development of the automotive industry, lightweight has become one of the indispensable requirements for automotive performance design. Steel-aluminum hybrid bodies have been used to reduce the weight of the entire vehicle, but also creates a problem, where the melting points of steel and aluminum are very different, thus difficult to weld the two material sheets together using traditional welding methods [1]. Since the self-piercing riveting (SPR) is a cold-formed fastening technology, high melting point of the sheets is not required, thus can be used as an alternative to traditional welding process in the connection of steel and aluminum sheets.

A good SPR joint quality is helpful to the stability of the joint, thus studying the effect of the different process parameters on the joint quality is important. The main factors that affect the quality of SPR joints are the geometry of the rivet, type of the die, thickness and material of the sheets, etc. [2]. When the thickness and material of the sheets are constant, the geometric parameters of the rivet and die result in a great effect on the quality of the joint. Many researchers have studied the geometric parameters of the rivet and die.

Zhao et al. [3] studied the effect of rivet length, die diameter, die depth, and the interaction between these parameters on the interlock value and the minimum remaining thickness of bottom through a combination of experiment and simulation, and regression analysis method is considered to predict riveting quality. Karathanasopoulos et al. [4] studied the relationship between the interlock value of joints and the geometry of rivets and dies, and used the neural network model to classify the geometry of the various rivets and dies that can successfully form the joint. Uhe et al. [5] improved the geometric shape of the rivet to connect both the upper and lower sheets made of high-strength steel materials, the upper sheet

✉ Dewen Kong
Kongdw19@mails.jlu.edu.cn

¹ State Key Laboratory of Automotive Simulation and Control, Jilin University, Changchun 130022, Jilin, People's Republic of China

made of aluminum alloy, and the lower sheet made of high-strength steel materials. Deng et al. [6] performed quasi-static tensile experiments and simulations on SPR joints formed using flat dies and dies with pip, and discussed the effect of the geometry of the die on the peak load and energy absorption of the joints. Ma et al. [7] studied the effect of the four key parameters of rivet hardness, rivet length, die width, and die pip height on the riveting ability of steel-aluminum sheets and the mechanical properties of the joints. Zhao et al. [8] studied the effect of die pip height on the static mechanical properties of SPR joints, and concluded that a smaller pip height can get better joint stability. Casalino [9] studied the effect of rivet length, pip height, and their interaction on the punch force–displacement curve during the SPR forming process by designing DOE experiments. Pickin et al. [10] studied the effect of die geometrical parameters on the rivet shank flaring and concluded that increasing the diameter and reducing the depth of die increase the rivet shank flaring correspondingly. Xu [11] used the ANOVA method to study the effects of rivet length and die type on joint undercut, bottom remaining thickness, and rivet flaring. Sun and Khaleel [12] studied the effect of rivet length and diameter on joint strength and found that the joint strength increases with increased rivet diameter and length. Han et al. [13] analyzed and optimized nine die parameters by setting up orthogonal experiments, hence selected a die parameter combination that can obtain the best joint quality. However, most of these studies only focus on typical rivet and die geometric parameters. Few studies on the effect of rivet blade angle and rivet shank thickness on joint quality exist.

With the development of finite element technology, many researchers used various finite element software to model and simulate SPR successfully. Hönsch et al. [14] used the Simufact Forming software to simulate the failure modes of SPR joints under different angle loads. Casalino et al. [15] used the LS-DYNA software to simulate the forming process of SPR, and the obtained joint section size and punch force–displacement curve can form good contrast with the experiment. Bouchard et al. [16] used the Forge2005® software to establish a 2D SPR model and used the kill element method to simulate the element failure. Porcaro et al. [17, 18] used the LS-DYNA software to simulate the SPR forming process and used r-adaptivity method to solve the problem of element distortion caused by rivet penetrating the sheet. A new algorithm was developed to map the stress and strain field on the formed 2D SPR model to the 3D model. Atzeni et al. [19] used Abaqus to establish a 2D SPR model and successfully simulated its forming process and shear failure. Lin et al. [20] used the Simufact Forming software to model the forming process and cross-tension testing of SPR joints. Obtained cross-sectional dimensions and cross-tension strength were in good agreement

with the experiment. The cross-tension strength of SPR joints was successfully predicted using extreme gradient boosting decision tree (XGBoost) algorithm.

The above methods used the 2D axisymmetric method to establish the SPR finite element model. The 2D axisymmetric method is a quick way of modeling, but too ideal. When simulating some extreme conditions (such as when an angle between rivet and sheet exists), this method cannot simulate the SPR forming process accurately. In addition, to simulate the failure of the formed joint, rotating the formed 2D geometric model into a 3D model first is necessary, then an external program is used to map the stress and strain information after the 2D forming to the new 3D model. However, most commercial finite element software does not integrate this function, which brings inconvenience to simulation researchers who are not familiar with the secondary development of finite element. Directly establishing a 3D finite element model does not impose axisymmetric constraints, can simulate the riveting process more objectively, and realize the integrated simulation of SPR joints from forming to damage. Therefore, studying the 3D finite element modeling of SPR is necessary.

Many researchers have used traditional method to establish 3D SPR finite element models [21–23] and used the element deletion method to simulate the material failure of the upper sheet due to large deformation during the rivet piercing process. Therefore, deleting too much sheet elements near the rivet shank, resulting in a void around it, which is not conducive to the observation of cross-section information, thus deletion of material causes loss of mass and energy, shape response is underestimated, and the deformation mode is incorrectly predicted. The smooth particle Galerkin (SPG) [24, 25] algorithm can effectively solve the problem on material failure caused by the rivet piercing the upper sheet during the joint forming process. Huang et al. [26, 27] applied the SPG algorithm to the SPR simulation for the first time using a combination of SPG and finite element model (FEM) to establish SPR 3D finite element model and researched the impact of critical parameters on the model through sensitivity study.

In recent years, the technique for order preferences by similarity to ideal solution (TOPSIS) [28] and entropy weight method [29, 30] have been well applied in the field of automotive lightweight, but researchers have not used these methods in the field of SPR. Both TOPSIS and entropy method are multicriteria decision-making (MCDM) methods. When SPR involves multiple evaluation indicators, MCDM can be used as a simple and systematic method in joint analysis and process optimization. Therefore, this paper applied MCDM method to SPR research and to select a combination that can meet multiple evaluation indicators at the same time from a variety of rivet and die combinations.

This paper established 3D finite element model by SPG algorithm to study the effect of rivet length, rivet shank thickness, rivet blade angle, die diameter, and die depth on the cross-sectional dimensions and cross-tension strength of SPR joints. First, a finite element model was established and verified with experimental results to prove the accuracy of the simulation. Second, the effects of the above five parameters on the cross-sectional dimensions and cross-tension strength were studied separately. Finally, a total of 32 sets of orthogonal experiments were designed according to different rivet and die combinations, and TOPSIS combined with entropy weight method was used to select a combination that can meet multiple evaluation indicators simultaneously.

2 Finite element analysis and experimental verification

2.1 Model description

2.1.1 Joint forming simulation

The commercial software, LS-DYNA, was used to establish the SPR 3D finite element model, where the cross-sectional view of the model is shown in Fig. 1. The punch, rivet, blank holder, AA5052 upper sheet, and HC340LA lower sheet and die can be seen from top to bottom. Among them, the punch, blank holder, and die were defined as rigid bodies, while the rivet and the upper and lower sheets were defined as deformable bodies. The thicknesses of the upper and lower sheets were 2 mm and 1.5 mm, respectively. According to references [27, 31], the average mesh size was set to 0.16 mm × 0.2 mm × 0.2 mm. Since the SPG algorithm significantly increases the simulation calculation time, the elements that may be severely deformed on the AA5052 sheet were set as SPG particles, and the elements far away from riveting area still modeled by FEM. The SPG particles

and FEM were coupled by common nodes that can not only guarantee the calculation accuracy, but also save the calculation resources.

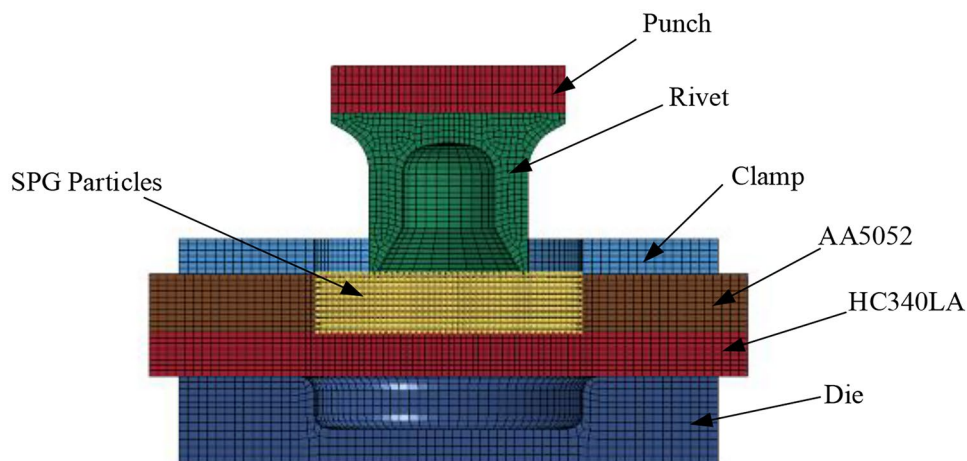
In the SPR forming simulation process, the punch and blank holder were only allowed to move longitudinally, and the die was subject to fixed constraints with 6 degrees of freedom. To prevent a gap between the upper and lower sheets, a vertical downward force of 3500 N was set on the blank holder to clamp the upper and lower sheets through the interaction with the die from the beginning of the simulation. The pressing speed of the punch was set to 130 mm/s to make the simulation and experiment consistent. Used node to surface contact algorithm between SPG particles and rivet, and between SPG particles and lower sheet, while surface to surface contact algorithm was used between other parts. This paper did not focus on the effect of friction on the joint, and the rivets and sheets used in the experiment were not treated with a special coating process. The coefficient of friction (CF) for static and dynamic contact between all components was set to 0.2 based on the settings in other references [1, 4]. Mass scaling was used to reduce the calculation time of the CPU during the simulation.

In this paper, the bond fracture algorithm [32, 33] was used to define the failure criterion of the SPG particles area. In the bond failure criterion, when the average effective plastic strain between two adjacent particles reaches the critical value, they are disconnected during the search of adjacent particles. According to the material properties of AA5052 [34], the maximum plastic strain under the quasi-static tensile test is 0.2. Therefore, the critical value of bond fracture was set to 0.2.

2.1.2 Cross-tension simulation

In this paper, the integrated modeling of SPR joints from forming to cross-tensioning was adopted, which can ensure that the residual stresses and plastic strain fields generated

Fig. 1 Cross-section of the SPR model



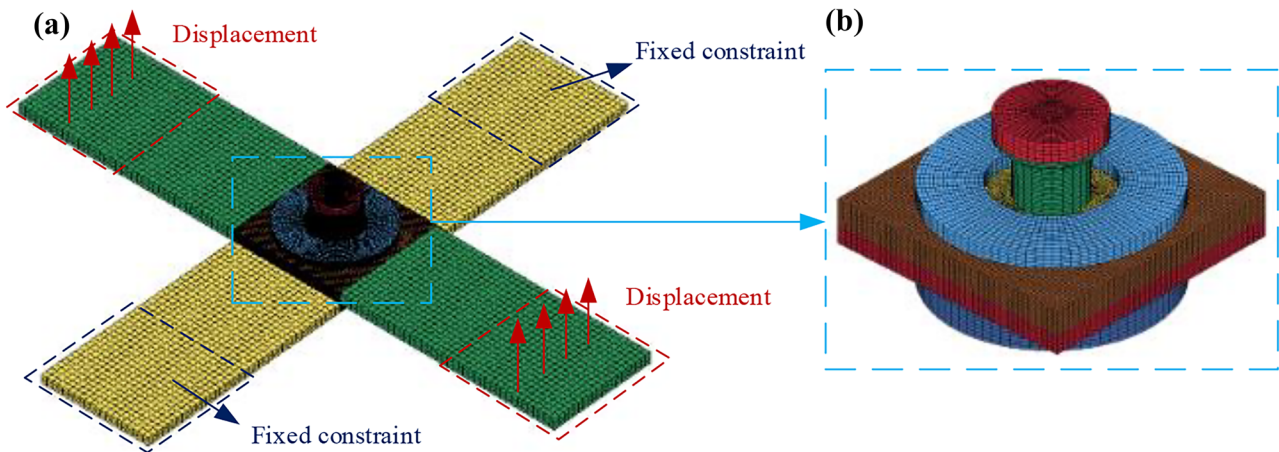


Fig. 2 (a) Cross-tension FEM. (b) Joint forming part

from the SPR forming simulation will not be lost and using complex simulation methods such as restarting is no longer necessary. A cross-tension FEM was established. The material properties, contact type, and friction size of the forming area were consistent with the settings in the previous section. The bond fracture failure criterion was set for the SPG area of the upper sheet, and no material failure was set for the other parts. To save the simulation time, a larger mesh size can be set for the sheets away from the forming area. The mesh size of this part is set to $1\text{ mm} \times 1\text{ mm} \times 0.5\text{ mm}$ and connected to the joint forming area through the contact type: CONTACT_TIED_SURFACE_TO_SURFACE.

When the forming simulation was completed, the displacement in the opposite direction for the punch, blank holder, and die is set to not participate in the subsequent cross-tension simulation. In the cross-tension simulation, the lower sheet was fixed, and the upper sheet was pulled upward at a speed of 10 mm/min to simulate the real tension process. The simulation ended until the joint was completely broken. The established FEM is shown in Fig. 2.

2.2 Material constitutive and properties

Johnson–Cook constitutive equation was used to define the material properties of the sheets. Johnson–Cook can simulate the mechanical properties of material at different strain rates well. Since the experiments and simulations in this

paper were carried out at room temperature without considering the influence of temperature, the Johnson–Cook model can use simplified constitutive in Eq. (1):

$$\sigma = \left(A + B\varepsilon_p^n \right) \left(1 + C \ln \frac{\dot{\varepsilon}}{\dot{\varepsilon}_0} \right) \quad (1)$$

where A is the yield strength of the material, B is the work hardening modulus, ε_p is the equivalent plastic strain, n is the hardening index, C is the strain rate constant, $\dot{\varepsilon}$ is the equivalent plastic strain rate, and $\dot{\varepsilon}_0$ is the strain rate reference value.

The materials of the upper and lower sheets were AA5052 aluminum alloy and HC340LA high-strength steel, respectively. The specific material properties are shown in Table 1.

The rivet's material used in this paper was boron steel. The principal mechanical properties are shown in Table 2.

2.3 Experimental methods

The riveting equipment used in this paper was the EP-CTF-50 self-piercing riveting machine produced by EPRESS, as shown in Fig. 3. The riveting method was to lap the 2-mm thick AA5052 aluminum sheet and the 1.5-mm thick HC340LA steel sheet in the form of upper aluminum and lower steel and used a rivet in the middle to join the two sheets together. The size of the rivet used was

Table 1 Mechanical properties of the sheets' materials [34, 35]

Material	Density (g/cm^3)	Elastic modulus (MPa)	Poisson's ratio	Johnson–cook parameters			
				A (MPa)	B (MPa)	n	C
AA5052	2.68	6.40E+04	0.3	143.1	215.7	0.54	0.0046
HC340LA	7.81	2.10E+05	0.3	360	477	0.57	0.03

Table 2 Mechanical properties of the rivet [36]

Material	Density (g/cm ³)	Elastic modulus (MPa)	Poisson's ratio	Yield stress (MPa)	Ultimate stress (MPa)	Elongation (%)
Boron steel	7.85	2.00E+05	0.3	1520	1720	22

Ø5.3×5.5 mm, and the flat die used had a depth of 1.8 mm and a diameter of 9 mm. The geometries of the rivet and die are shown in Fig. 4.

Cross-tension experiment was performed on SPR joints. Specifically, the upper aluminum and lower steel sheets with the same length and width were stacked together in a cross shape. The riveting position was marked in the middle of the two sheets, used a rivet to join the two sheets together, manufactured into a cross-shaped SPR joint structure sample, as shown in Fig. 5. The upper and lower sheets were clamped by a special fixture and fixed them on the CMT4304 testing machine. The lower sheet was fixed, and the upper sheet was stretched axially at a speed of 10 mm/min until the joint was completely failed.

2.4 Model validation

The accuracy of the simulation model was verified by comparing the cross-section information and cross-tension results obtained by SPR simulation and experiment. Figure 6 shows

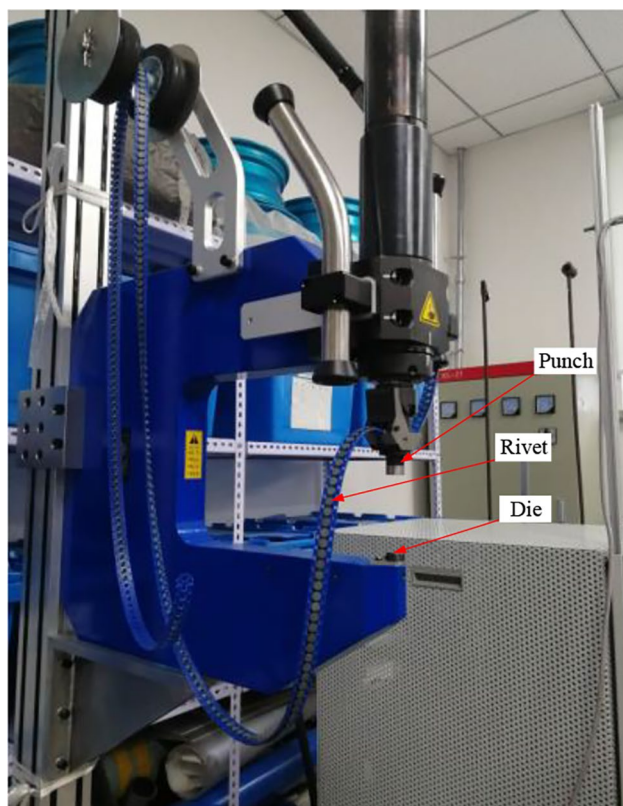


Fig. 3 SPR riveting machine

the cross-section comparison between SPR experiment and simulation. The left side is the cross-section obtained by the experiment, and the right side is the cross-section obtained by the simulation. The amount of undercut and the remaining thickness of the bottom were used as the evaluation indicators of the SPR forming result. As shown in Table 3, the error between the undercut amount and the remaining thickness of the bottom obtained from simulation and experiment are within 10%, indicating that the simulation model established by SPG particles can reflect the cross-section information of SPR accurately. Among them, a part of cavity between the rivet and the upper sheet in simulation was observed, which was slightly different from the real cross section. This deviation can be explained as the excessive response of the bottom sheet during the rivet piercing process [26], which had little effect on the acquisition of key parameters.

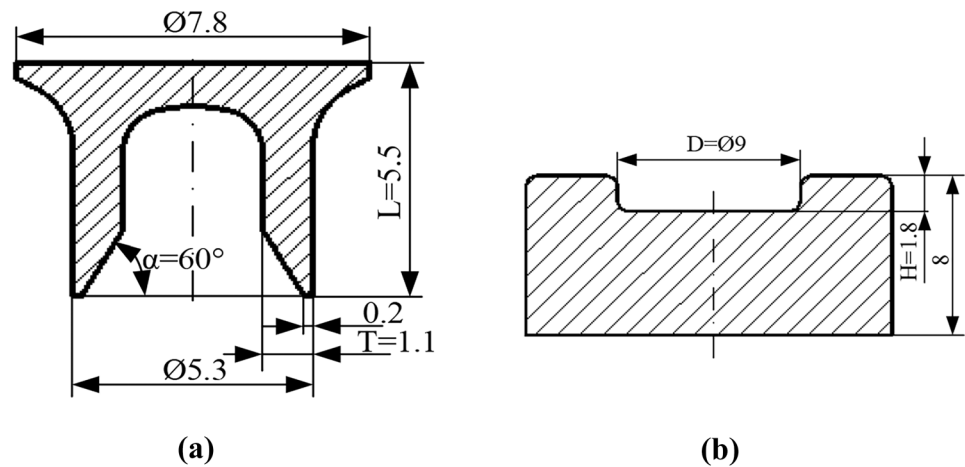
As shown in Fig. 7, the failure mode of the SPR joint obtained by the cross-tension simulation is consistent with the experiment result, where the upper sheet drives the rivet to pull out from the lower sheet.

The force–displacement curve comparison obtained by the simulation and experiment is shown in Fig. 8. The trends of the two curves are basically the same. Among them, the cross-tension strength of simulation and experiment are 2967.24 N and 3109 N, respectively, where the relative error is 4.6%. The failure displacement of simulation and experiment are 14.5 mm and 13.7 mm, respectively, where the relative error is 5.8%. The difference between the results can be attributed to the slight slippage between the fixture and sheets during the cross-tension experiment, whereas the finite element simulation will not encounter this problem. However, the cross-tension strength and failure displacement errors between simulation and experiment are both within 10%, indicating that the simulation model established by SPG particles can simulate the cross-tension result of SPR effectively.

3 Effect of rivet and die parameters on the quality of SPR joints

This section used finite element simulation to study the effect of rivet length (L), rivet blade angle (α), rivet shank thickness (T), die diameter (D), and die depth (H) on the quality of SPR joints (cross-sectional dimensions and cross-tension strength). Figure 9 shows that the evaluation indicators of SPR cross-sectional dimensions are undercut (du),

Fig. 4 Geometries of the rivet and die (dimensions in mm). (a) Rivet, (b) Die



bottom remaining thickness (db) and rivet shank flaring (df). The evaluation indicator of the cross-tension result is the cross-tension strength.

Table 4 shows the 11 designed sets of rivet and die combinations. The rivet and die combination that has been simulated and verified by the experiment was selected as the benchmark S0 (Fig. 4), while other combinations only have a single parameter change based on S0. Joint forming simulation was performed for each combination first, and the cross-tension simulation is performed for them.

3.1 Effect of rivet and die parameters on the cross-sectional dimensions

3.1.1 Effect of rivet length

SPR forming simulation performed on the rivet and die combination S0, S1, S2, and the cross-sectional view are shown in Fig. 10:

As shown in Fig. 10, when the rivet length (L) increases, du and df increase and db decreases. When L

is too short, the ability of the rivet to overcome the bending resistance of the sheets is weak, thus df is small. Most of the rivet shank are stuck in the upper sheet during rivet penetration, hence the rivet cannot form a good interlock with the lower sheet, thus du is small. Although riveting can be achieved in this case, the performance of the joint is weakened, the risk of separation of the upper and lower sheets of the joint are increased, and the tensile strength of the joint is reduced. As L increases, the amount of rivet penetration into the lower sheet increases. At this time, the value of du is mainly determined by df , where increase df will increase du . With increased L , the db shrinks very obviously, indicating that if L is too long, resulting in a risk of breaking the lower sheet.

3.1.2 Effect of rivet blade angle

SPR forming simulation performed on the rivet and die combination S3, S4, and the cross-sectional view are shown in Fig. 11:

Fig. 5 Diagram of cross-tension specimen: (a) Schematic, (b) Experimental

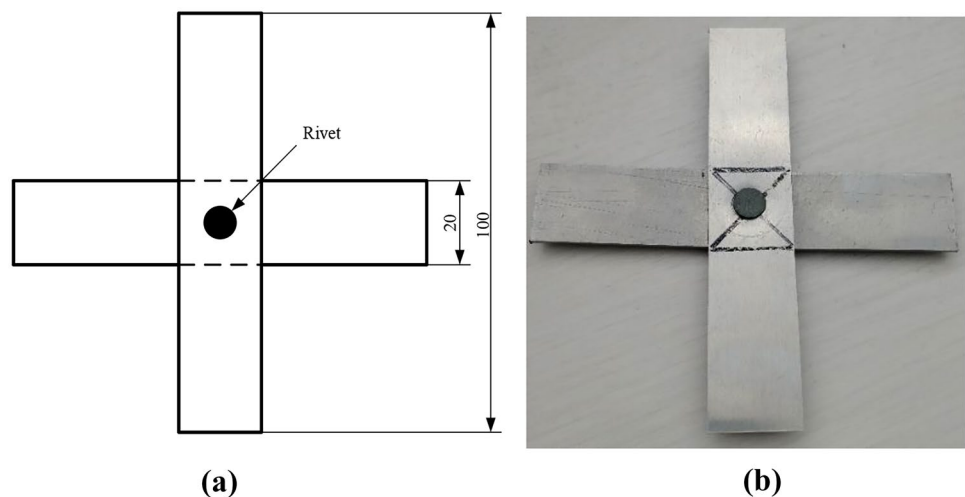
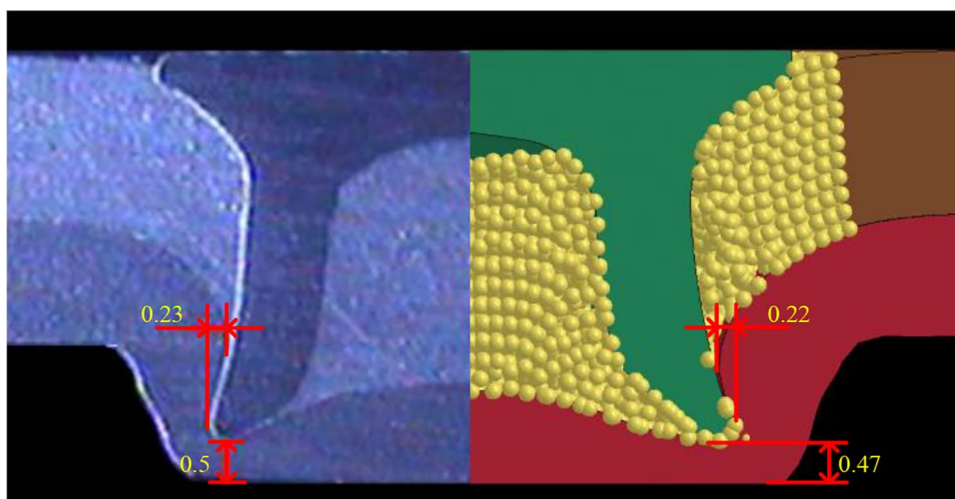


Fig. 6 Cross-sectional comparison diagram of SPR experiment and simulation



As shown in Figs. 10b and 11, when the rivet blade angle (α) increases, du , df , and db also increase because as the larger value of α , the sharper the rivet blade and the stronger the ability of rivet to penetrate the sheets. During the forming process, the die forms a protrusion in the middle of the lower sheet, which increases the tendency of the rivet shank to expand in the radial direction and increase the penetration of the rivet in the radial direction, thereby reducing the penetration of the rivet in the axial direction. Therefore, the values of du , df , and db increase.

3.1.3 Effect of rivet shank thickness

SPR forming simulation performed on the rivet and die combination S5, S6, and the cross-sectional view are shown in Fig. 12:

As shown in Figs. 10b and 12, when the rivet shank thickness (T) increases from 1 to 1.1 mm, du , df , and db increase accordingly, indicating that a proper increase of T can make the rivet shank expand radially more easily during the penetration process of the rivet. When T changes from 1.1 mm to 1.2 mm, du and df slightly increase, while db decreases. Thus, when T is too large, the ability of the rivet shank to resist deformation becomes stronger, which causes the ability of the rivet shank to expand in the radial direction is relatively weakened, so du and df only slightly increase. At this time, the rivet is mainly penetrated in the axial direction, and the penetration depth of the lower sheet increases, thus db is reduced.

Table 3 Comparison of the results of experiment and simulation

Evaluation index	Experiment	Simulation	Error (%)
Undercut (mm)	0.23	0.22	4.50%
Remaining thickness of bottom (mm)	0.5	0.47	6.40%

3.1.4 Effect of die diameter

SPR forming simulation performed on the rivet and die combination S7, S8, and the cross-sectional view is shown in Fig. 13:

As shown in Figs. 10b and 13, the increased die diameter (D), du decreases, and df and db increase. When D is 8 mm, the volume ratio of the die cavity to the rivet is about 1, that is, the flowing sheet material after the rivet penetrates the upper and lower sheets can completely fill the die cavity, hence the rivet can penetrate the lower sheet more deeply, which makes the db relatively small. Since the side wall of the die provides resistance to the radial flow of the sheet, the rivet shank is restrained from continuing to expand in the radial direction to a certain extent, thus the df is relatively small. At the same time, the contact between the sheet and rivet shank is tighter, making the du relatively large. When

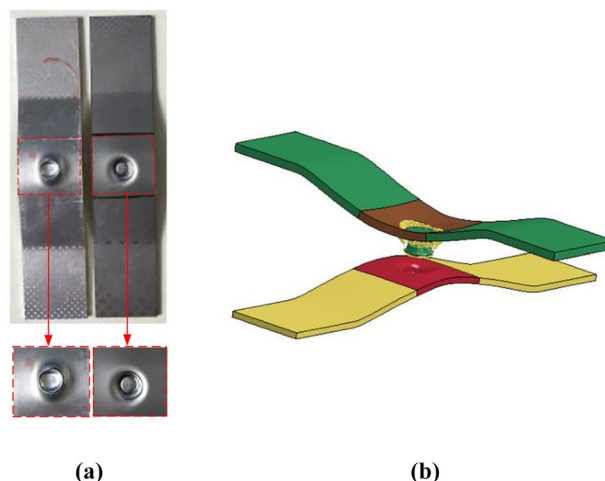


Fig. 7 Comparison of the joint failure modes: (a) Experimental, (b) Simulation

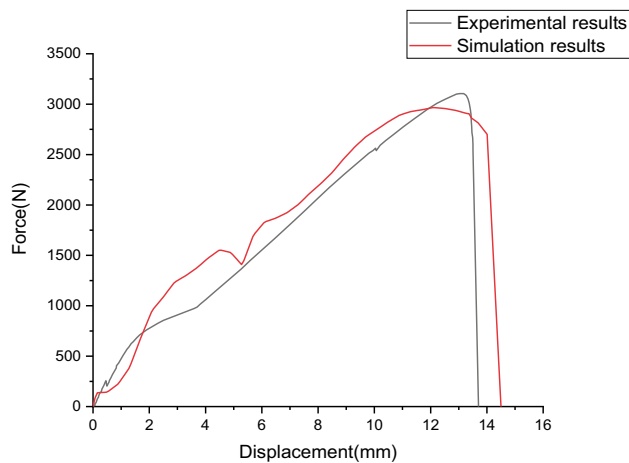


Fig. 8 Comparison of force–displacement curves between simulation and experiment

D continues to increase, the die space increases, where the deformed sheet material can flow in the radial direction during the riveting process. Since the radial resistance of the die and sheets to the rivet is reduced, the rivet shank tends to expand radially and weakens the depth of penetration into the lower sheet, so that df and db increase. At the same time, the radial flow of the sheets increases the gap between the rivet shank and the lower sheet, thus du is reduced.

3.1.5 Effect of die depth

SPR forming simulation performed on the rivet and die combination S9, S10, and the cross-sectional view are shown in Fig. 14:

As shown in Figs. 10b and 14, the increased die depth (H) result in the decreased in du and df , and increased in db . Because with the increase in H , the die provides more space for the sheet material to flow in the axial direction and since the length of the rivet is fixed, the depth of penetration of the rivet into the lower sheet inevitably decreases, thus db increases. At the same time, the increase in H reduces the expansion of the rivet shank in the radial direction, so du and df decrease.

Fig. 9 Quality evaluation indicators of the SPR cross-section

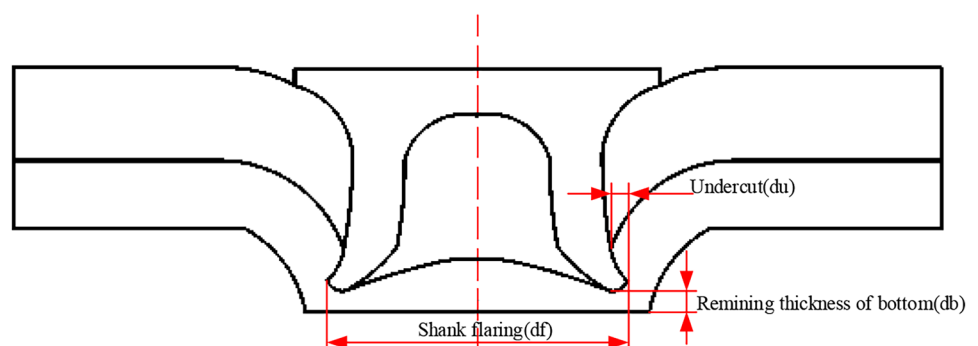


Table 4 Different parameter combinations of rivet and die

Joint no	L (mm)	α (°)	T (mm)	D (mm)	H (mm)
S0	5.5	60	1.1	9	1.8
S1	5	60	1.1	9	1.8
S2	6	60	1.1	9	1.8
S3	5.5	50	1.1	9	1.8
S4	5.5	55	1.1	9	1.8
S5	5.5	60	1	9	1.8
S6	5.5	60	1.2	9	1.8
S7	5.5	60	1.1	8	1.8
S8	5.5	60	1.1	10	1.8
S9	5.5	60	1.1	9	1.7
S10	5.5	60	1.1	9	1.9

3.2 Effect of rivet and die parameters on the cross-tension strength

Figure 15 shows the two main types of cross-tension failure modes of SPR joints, namely, rivet pull-out failure mode and upper sheet fracture mode.

SPR cross-tension simulation performed on the rivet and die combinations is shown in Table 4, where the upper sheet fracture failure occurred in combination S2 and the rivet pull-out failure occurred in other combinations. The cross-tension strength value is recorded in Fig. 16.

As shown in Fig. 16a, when the rivet length (L) is 5 mm and 5.5 mm, increased L result in the rapid increase in cross-tension strength. When L reaches 6 mm, the cross-tension strength increases slowly because the failure mode of the joint is the upper sheet fracture failure. The upper sheet is broken and the rivet is stuck in the lower sheet, as shown in Fig. 17. Once the upper sheet breaks in the lap sequence of upper aluminum and lower steel sheets, the cross-tension strength will not change much.

As shown in Fig. 16b, increased rivet blade angle (α) results in the increase in cross-tension strength first and then decreases. According to the analysis results of the previous section, the increase in α will increase the du of the joint, which will increase the cross-tension strength. But at the

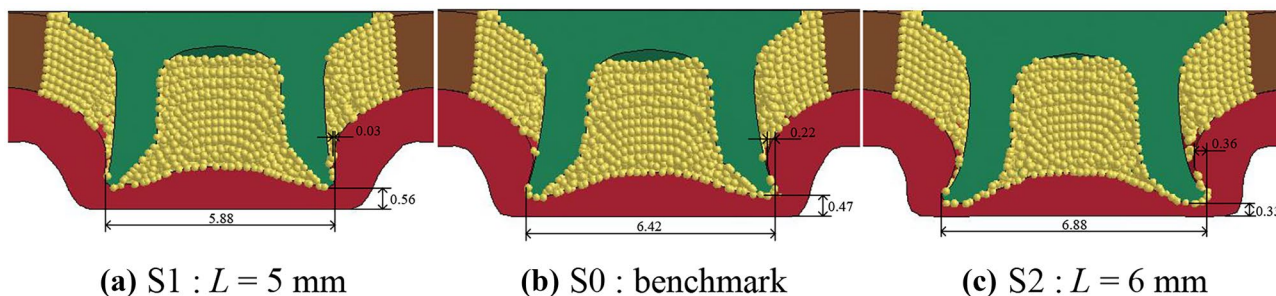


Fig. 10 Cross-sectional view of joints with different rivet length. (a) S1: $L = 5$ mm, (b) S0: benchmark, (c) S2: $L = 6$ mm

same time, the increase in α will make the rivet blade thinner and weaken the ability of rivet to resist stretching. Therefore, when α is 60° , the cross-tension strength becomes smaller than the results from the first two angles are obtained.

As shown in Fig. 16c, increased rivet shank thickness (T) results in the increased cross-tension strength because the increase in T will increase du correspondingly, making the rivet less likely to be pulled out by the upper sheet.

As shown in Fig. 16d, when die diameter (D) is 8 mm, the cross-tension strength is relatively small. When D is from 9 to 10 mm, the cross-tension strength decreases as D increases. Under normal circumstances, with the increase in D , du correspondingly decreases, and the cross-tension strength should also decrease correspondingly. However, Fig. 18 shows that when D is 8 mm, although the failure mode is still that the rivet is pulled out with the upper sheet during stretching, the upper sheet deforms seriously, resulting in a smaller cross-tension strength.

As shown in Fig. 16e, increased die depth (H) results in gradual decrease in cross-tension strength because the increase in H will lead to the corresponding decrease in du . In the case of cross-tension, the rivet is more easily pulled out by the upper sheet.

The failure mode has a great effect on the value of the cross-tension strength. When the rivet pull-out failure of the joint occurs, the cross-tension strength usually increases with the increase in du . When the upper sheet fracture of the joint occurs, the cross-tension strength will not change too much.

4 MCDM based on entropy weight TOPSIS method

The evaluation of joint quality mainly includes undercut (du), bottom remaining thickness (db), rivet shank flaring (df), cross-tension strength, etc. Good joint quality needs to take these factors into consideration at the same time. Therefore, this paper used TOPSIS combined with entropy method to select a combination that can meet all evaluation indicators from a variety of rivet and die combinations.

4.1 Orthogonal test

To minimize the number of SPR simulations required, orthogonal arrays were used to design rivet and die parameters. Using the L32 (4^5) orthogonal table to design an orthogonal test with five factors and four levels. A total of 32 sets of rivet and die combinations and simulation results are shown in Table 5.

For a flat die, the du and db of the joint show an opposite trend [37], therefore, a smaller db should be used to obtain a larger du . However, if db is too small, the risk of the lower sheet being penetrated increases. Therefore, it should ensure that db is greater than 0.2 mm [38]. The db obtained by all combinations in Table 5 is greater than 0.2 mm, and all meet the requirements of the joint for db . This paper aims to determine the larger du , df ,

Fig. 11 Cross-sectional view of joints with different rivet blade angle. (a) S3: $\alpha = 50^\circ$, (b) S4: $\alpha = 55^\circ$

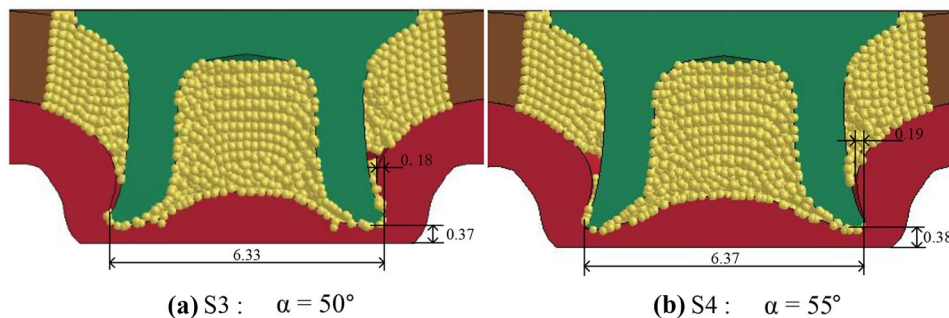
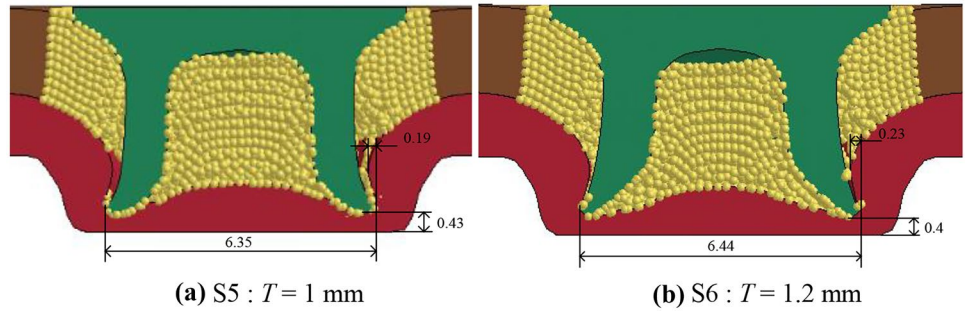


Fig. 12 Cross-sectional view of joints with different rivet shank thickness. (a) S5: $T=1$ mm, (b) S6: $T=1.2$ mm



cross-tension strength, and smaller db . According to the results in Table 5, the 28th group is the optimal combination for du , the 21st and the 30th groups are the optimal combination for db , the 30th group is the optimal combination for df , and the 25th group is the optimal combination for cross-tension strength. None of the above combinations can meet the four indicators at the same time. To select a rivet and die combination that can make each evaluation indicator as good as possible, this paper used TOPSIS combined with entropy weight method to analyze the results.

4.2 TOPSIS combined with entropy weight method

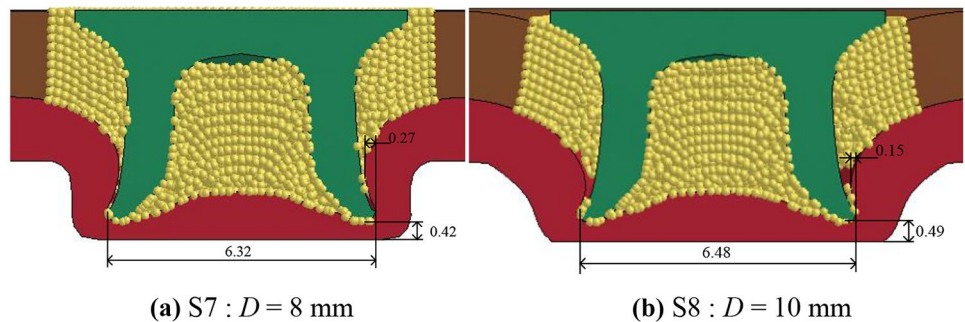
TOPSIS is a practical method to solve the MCDM problem by measuring the Euclidean distance and ranking the possible alternatives [28]. Specific steps are as follow:

Since the target contains both very large and small (db) indicators, for the convenience of subsequent analysis, the indicator data are normalized first and converted into very large and normalized indicator data, and the normalized data are defined as the decision matrix of the TOPSIS method, which can be expressed as:

$$X = \begin{pmatrix} x_{11} & x_{12} & \dots & x_{1m} \\ x_{21} & x_{22} & \dots & x_{2m} \\ \vdots & \vdots & \ddots & \vdots \\ x_{n1} & x_{n2} & \dots & x_{nm} \end{pmatrix} \tag{2}$$

where n represents the number of evaluation objects and m represents the number of evaluation indicators.

Fig. 13 Cross-sectional view of joints with different die diameter. (a) S7: $D=8$ mm, (b) S8: $D=10$ mm



To eliminate the influence of the dimensions of different indicator data, the above matrix is standardized, where the equation is:

$$z_{ij} = \frac{x_{ij}}{\sqrt{\sum_{i=1}^n x_{ij}^2}} \tag{3}$$

Finally, the evaluation matrix after normalization and standardization is represented by Z and can be obtained as follow:

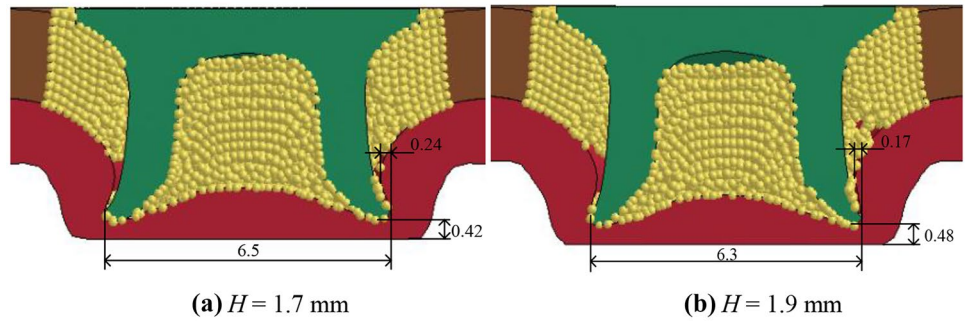
$$Z = \begin{pmatrix} z_{11} & z_{12} & \dots & z_{1m} \\ z_{21} & z_{22} & \dots & z_{2m} \\ \vdots & \vdots & \ddots & \vdots \\ z_{n1} & z_{n2} & \dots & z_{nm} \end{pmatrix} \tag{4}$$

To describe the importance of each evaluation indicator objectively, the entropy weight method was used to weight each indicator, and the concept of information entropy was introduced. Information entropy is the expectation of the amount of information. The smaller the information entropy of an indicator, the greater the amount of information that the indicator can provide, the greater the role it plays in the comprehensive evaluation, and the greater the weight. The E_j equation for information entropy is as follow:

$$E_j = -\ln(n)^{-1} \sum_{i=1}^n p_{ij} \ln p_{ij} \tag{5}$$

where $p_{ij} = \frac{z_{ij}}{\sum_{i=1}^m z_{ij}}$ is the result of standardized processing.

Fig. 14 Cross-sectional view of joints with different die depth. (a) $H=1.7$ mm, (b) $H=1.9$ mm



The weight of each indicator is calculated according to the information entropy:

$$w_j = \frac{1 - E_j}{\sum_{j=1}^n (1 - E_j)} \quad (6)$$

where $w_j \in [0, 1]$, $\sum_{j=1}^n w_j = 1$. The weight coefficient and information entropy of each indicator are obtained using the entropy weight method shown in Table 6.

Combining TOPSIS and entropy method to construct weighted standardized matrix:

$$V = (v_{ij})_{n \times m} = w_j \times z_{ij} \quad (7)$$

$$\begin{cases} V^+ = (v_1^+, v_2^+, \dots, v_m^+) \\ V^- = (v_1^-, v_2^-, \dots, v_m^-) \end{cases} \quad (8)$$

In the equation, V^+ , V^- denote the ideal solution set and the negative ideal solution set respectively. The ideal solution and negative ideal solution equation of the specific j indicator are as follows:

$$\begin{cases} v_j^+ = \max_i \{v_{ij}, j = 1, 2, \dots, n\} \\ v_j^- = \min_i \{v_{ij}, j = 1, 2, \dots, n\} \end{cases} \quad (9)$$

The Euclidean distance between each alternative and the ideal solution and the negative ideal solution are:

$$\begin{cases} D_i^+ = \sqrt{\sum_{j=1}^m (v_{ij} - v_j^+)^2} \\ D_i^- = \sqrt{\sum_{j=1}^m (v_{ij} - v_j^-)^2} \end{cases} \quad (10)$$

The relative closeness of each alternative to the negative ideal solution can be defined as the relative closeness coefficient, which can be used as a comprehensive evaluation index to determine the optimal alternative. The relative closeness coefficient calculation formula is:

$$S_i = \frac{D_i^-}{D_i^+ + D_i^-} \quad (11)$$

In this paper, S_i represents the relative closeness coefficient of the i -th rivet and die combination. The larger the value, the better the joint quality of the combination.

The results of the relative closeness coefficient of each rivet and die combination calculated by TOPSIS combined entropy weight method are shown in Fig. 19. The relative closeness coefficient value of combination 30 is the largest, indicating that the combination 30 with rivet length of

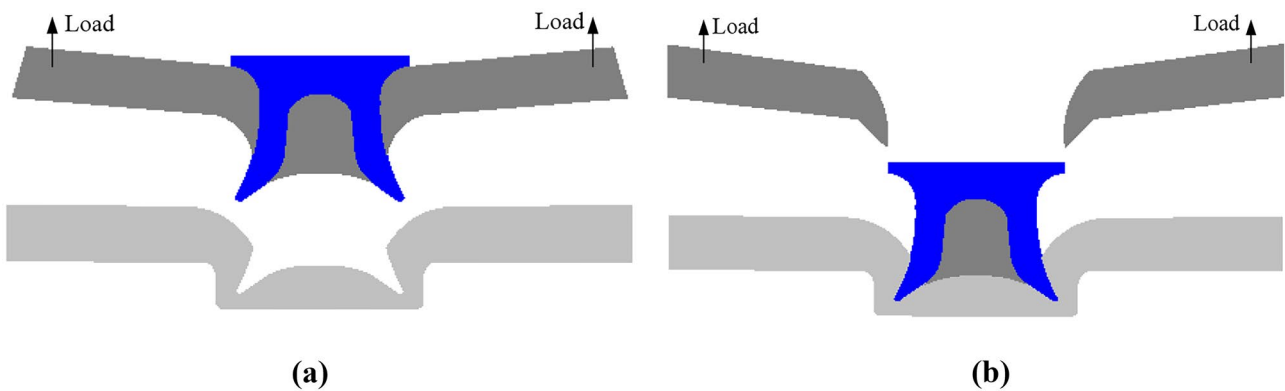


Fig. 15 Cross-tension failure modes of the SPR joints. (a) Rivet pull-out failure mode. (b) Upper sheet fracture mode

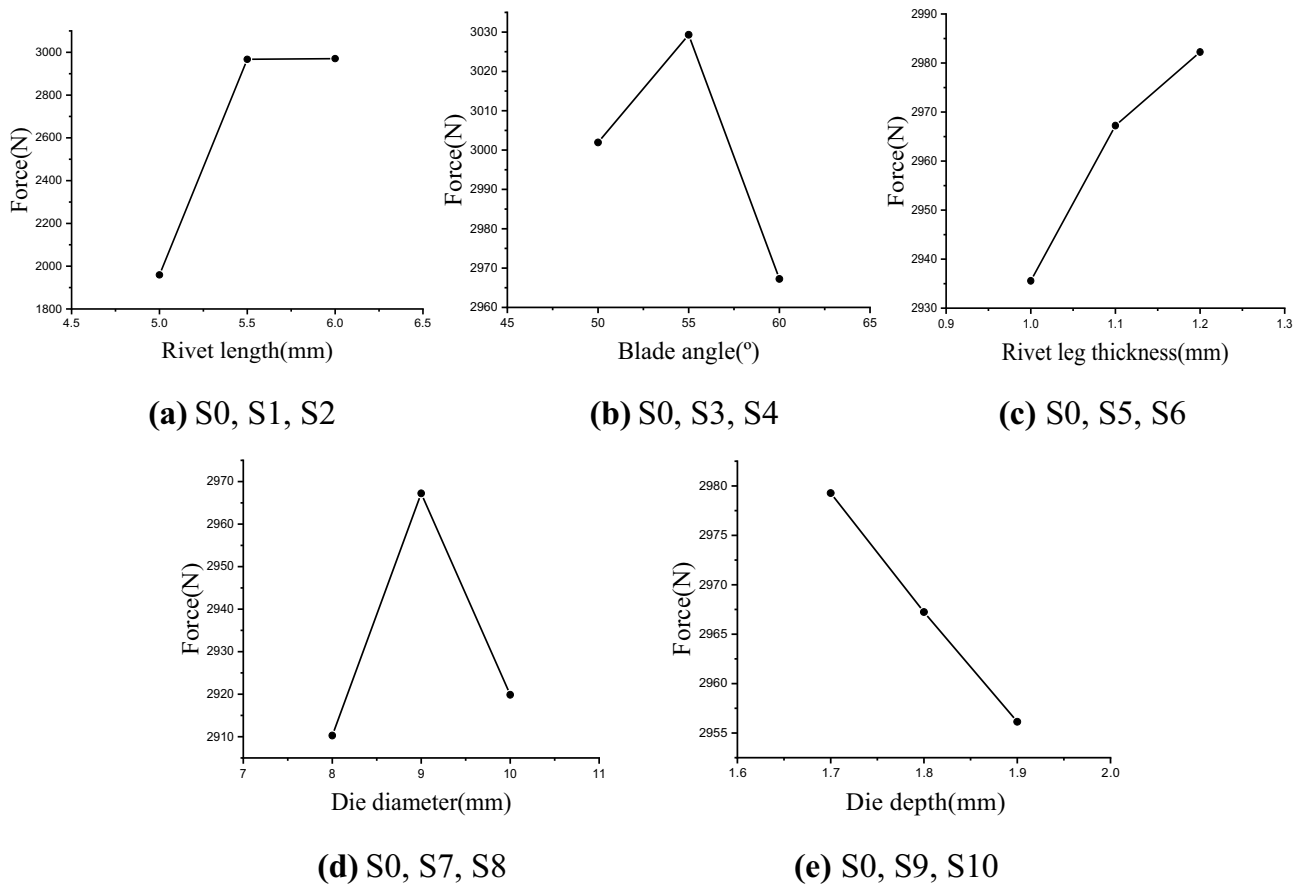


Fig. 16 Cross-tension strength of different rivet and die combinations. (a) S0, S1, S2, (b) S0, S3, S4, (c) S0, S5, S6, (d) S0, S7, S8, (e) S0, S9, S10

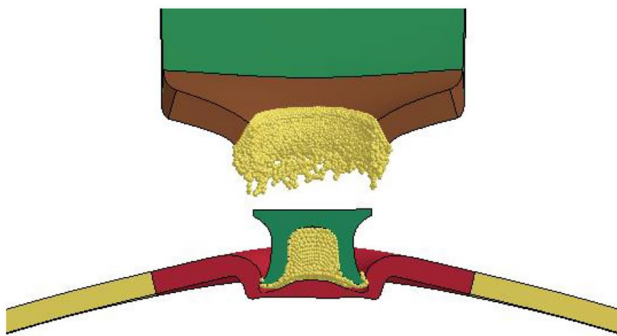


Fig. 17 Cross-tension failure mode of SPR when L is 6 mm

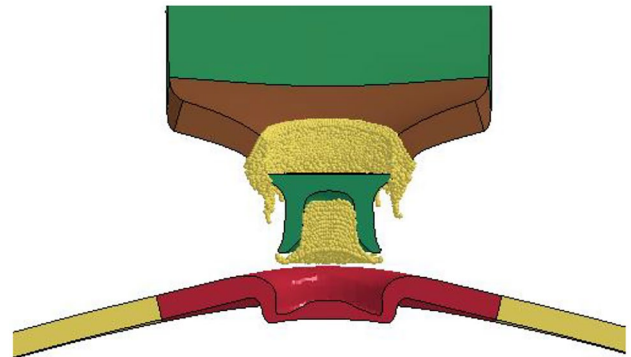


Fig. 18 Cross-tension failure mode of SPR when D is 8 mm

Table 5 Orthogonal table of rivet and die combinations and simulation results

Run32	<i>L</i>	α	<i>T</i>	<i>D</i>	<i>H</i>	du(mm)	db(mm)	df(mm)	Tension(N)
1	5	45	0.9	8	1.7	0.04	0.48	5.77	1984.63
2	5	50	1	9	1.8	0	0.54	5.78	1909.59
3	5	55	1.1	10	1.9	0	0.58	5.71	1877.42
4	5	60	1.2	11	2	0.01	0.67	5.79	1990.21
5	5	45	0.9	9	1.8	0	0.53	5.72	1905.72
6	5	50	1	8	1.7	0.08	0.51	5.87	2107.03
7	5	55	1.1	11	2	0	0.64	5.65	1828.61
8	5	60	1.2	10	1.9	0	0.62	5.85	1962.94
9	5.5	45	1	10	2	0.05	0.41	5.98	2038.74
10	5.5	50	0.9	11	1.9	0.07	0.47	6.21	2035.38
11	5.5	55	1.2	8	1.8	0.28	0.42	6.28	2983.64
12	5.5	60	1.1	9	1.7	0.25	0.43	6.53	3000.08
13	5.5	45	1	11	1.9	0.05	0.43	6.13	2031.49
14	5.5	50	0.9	10	2	0.04	0.42	6.07	1997.2
15	5.5	55	1.2	9	1.7	0.26	0.41	6.54	2973.37
16	5.5	60	1.1	8	1.8	0.25	0.42	6.31	2931.68
17	6	45	1.2	8	2	0.34	0.28	6.39	3019.04
18	6	50	1.1	9	1.9	0.37	0.29	6.75	3050.73
19	6	55	1	10	1.8	0.25	0.35	6.81	2978.09
20	6	60	0.9	11	1.7	0.18	0.41	6.91	2903.66
21	6	45	1.2	9	1.9	0.39	0.26	6.72	3100.35
22	6	50	1.1	8	2	0.37	0.31	6.45	3020.73
23	6	55	1	11	1.7	0.26	0.37	6.93	2945.11
24	6	60	0.9	10	1.8	0.24	0.37	6.8	2923.14
25	6.5	45	1.1	10	1.7	0.39	0.27	7.17	3136.88
26	6.5	50	1.2	11	1.8	0.35	0.3	7.36	2985.94
27	6.5	55	0.9	8	1.9	0.35	0.34	6.48	2856.02
28	6.5	60	1	9	2	0.43	0.31	7.02	2905.51
29	6.5	45	1.1	11	1.8	0.33	0.28	7.09	3029.8
30	6.5	50	1.2	10	1.7	0.42	0.26	7.46	3040.68
31	6.5	55	0.9	9	2	0.33	0.32	6.83	2976.49
32	6.5	60	1	8	1.9	0.38	0.33	6.57	2887.23

Table 6 Weight coefficient and information entropy of each evaluation indicator

Performance	Weight coefficient (w_j)	Information entropy (E_j)
Undercut (du)	0.7085	0.8987
Bottom remaining thickness (db)	0.2472	0.9647
Rivet shank flaring (df)	0.0064	0.9991
Cross-tension strength	0.0379	0.9946

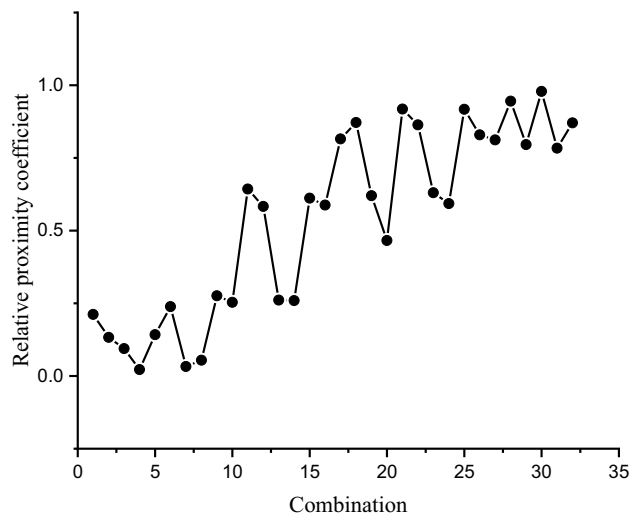


Fig. 19 Relative closeness coefficient of each rivet and die combination

6.5 mm, rivet blade angle of 50°, rivet shank thickness of 1.2 mm, die diameter of 10 mm, and die depth of 1.7 mm can get the best joint quality. In comparison with the benchmark combination, the combination of *du* increased by 90.9%, *db* decreased by 44.7%, *df* increased by 16.2%, and cross-tension strength increased by 2.5%.

5 Conclusion

This paper established the SPR 3D finite element model by SPG algorithm to analyze the effect of the important parameters of rivet and die (rivet blade angle, rivet shank thickness, rivet length, die diameter, and die depth) on the joint quality (cross-sectional dimensions and the cross-tension strength). A combination with the best joint quality was selected from a variety of rivet and die combinations by using TOPSIS combined with entropy weight method. The main conclusions were as follows:

1. The SPR FEM was established based on SPG particle algorithm, which can effectively solve the problem of material failure caused by the rivet piercing the upper sheet during the joint forming process. Thus, an integrated simulation model from rivet forming to cross-tensioning was further established, which can retain the plastic strain and residual stress information of the rivet and sheets during the joint forming process, and more accurately characterize the joint pulling damage and failure mechanism.
2. The effect of rivet and die parameters on cross-sectional dimensions and cross-tension strength was deeply studied. The undercut of the joint increases with the increase in rivet length, rivet blade angle, and rivet shank thickness, and decreases with the increase in die diameter and die depth. Under normal circumstances, the cross-tension strength increases with the increase in the undercut, but the failure mode of the joint has a great effect on the cross-tension strength.
3. The MCDM design model was established based on TOPSIS combined with entropy weight method, and the orthogonal table data of 32 sets of rivet and die combinations were analyzed. The results showed that the best joint quality can be obtained when a combination of rivet and die with a rivet length of 6.5 mm, rivet blade angle of 50°, rivet shank thickness of 1.2 mm, die diameter of 10 mm, and die depth of 1.7 mm were selected. In comparison with the benchmark combination, this combination had a 90.9% increase in undercut, 44.7% reduction in the remaining thickness of the bottom, 16.2% increase in rivet shank flaring, and 2.5% increase in the cross-tension strength. The method and result can provide references for the model selection and size design of rivets and dies.

Author contribution Dengfeng Wang: Funding acquisition, Writing. Dewen Kong: Methodology, Experiments, Software, Writing. Chong Xie: Methodology, Data curation. Shenhua Li: Software, Validation. Ling Zong: Experiments.

Funding This work was supported by the National Natural Science Foundation of China (number 51975244).

Availability of data and material The data used to support the findings of this study are included within the article.

Declarations

Ethics approval and consent to participate All authors participated in the research work.

Consent for publication All authors consent to publish.

Conflict of interest The authors declare no competing interests.

References

1. Abe Y, Kato T, Mori K (2006) Joinability of aluminium alloy and mild steel sheets by self piercing rivet. *J Mater Process Technol* 177:417–421
2. Haque R (2018) Quality of self-piercing riveting (SPR) joints from cross-sectional perspective: a review. *Arch Civ Mech Eng* 18:83–93
3. Zhao H, Han L, Liu Y, Liu X (2021) Modelling and interaction analysis of the self-pierce riveting process using regression analysis and FEA. *Int J Adv Manuf Technol* 113:159–176
4. Karathanasopoulos N, Pandya KS, Mohr D (2021) Self-piercing riveting process: prediction of joint characteristics through finite element and neural network modeling. *Journal of Advanced Joining Processes* 3. <https://doi.org/10.1016/j.jajp.2020.100040>
5. Uhe B, Kuball C, Merklein M, Meschut G (2020) Improvement of a rivet geometry for the self-piercing riveting of high-strength steel and multi-material joints. *Prod Eng Res Devel* 14:417–423
6. Deng J, Lyu F, Chen R, Fan Z (2019) Influence of die geometry on self-piercing riveting of aluminum alloy AA6061-T6 to mild steel SPFC340 sheets. *Adv Manuf* 7:209–220
7. Ma Y, Lou M, Li Y, Lin Z (2018) Effect of rivet and die on self-piercing rivetability of AA6061-T6 and mild steel CR4 of different gauges. *J Mater Process Technol* 251:282–294
8. Zhao J, Wan S, Li S (2011) Investigation of SPR mechanical performance with aluminum alloy sheet. *Appl Mech Mater* 37–38:599–602
9. Casalino G (2011) DOE analysis of the effects of geometrical parameters on the self-piercing riveting of aluminium alloy AA6060T4. *Key Eng Mater* 473:733–738
10. Pickin C, Young K, Tuersley I (2007) Joining of lightweight sandwich sheets to aluminium using self-pierce riveting. *Maters and Design* 28:2361–2365
11. Xu Y (2013) Effects of factors on physical attributes of self-piercing riveted joints. *Sci Technol Weld Join* 11:666–671
12. Sun X, Khaleel MA (2005) Performance optimization of self-piercing rivets through analytical rivet strength estimation. *J Manuf Process* 7:83–93
13. Han S, Li Z, Gao Y, Zeng Q (2014) Numerical study on die design parameters of self-pierce riveting process based on orthogonal test. *J Shanghai Jiaotong Univ (Sci)* 19:308–312

14. Hönsch F, Domitner J, Sommitsch C, Göttinger B (2020) Modeling the failure behavior of self-piercing riveting joints of 6xxx aluminum alloy. *J Mater Eng Perform* 29:4888–4897
15. Casalino G, Rotondo A, Ludovico A (2008) On the numerical modelling of the multiphysics self piercing riveting process based on the finite element technique. *Adv Eng Softw* 39:787–795
16. Bouchard PO, Laurent T, Tollier L (2008) Numerical modeling of self-pierce riveting — from riveting process modeling down to structural analysis. *J Mater Process Technol* 202:290–300
17. Porcaro R, Hanssen AG, Langseth M, Aalberg A (2006a) The behaviour of a self-piercing riveted connection under quasi-static loading conditions. *Int J Solids Struct* 43:5110–5131
18. Porcaro R, Hanssen AG, Langseth M, Aalberg A (2006b) Self-piercing riveting process: an experimental and numerical investigation. *J Mater Process Technol* 171:10–20
19. Atzeni E, Ippolito R, Settineri L (2009) Experimental and numerical appraisal of self-piercing riveting. *CIRP Ann Manuf Technol* 58:17–20
20. Lin J, Qi C, Wan H, Min J, Chen J, Zhang K (2021) Zhang L (2021) Prediction of cross-tension strength of self-piercing riveted joints using finite element simulation and XGBoost algorithm. *Chin J Mech Eng* 34:36. <https://doi.org/10.1186/s10033-021-00551-w>
21. Moraes JFC, Jordon JB, Su X, Barkey ME, Jiang C, Ilieva E (2019) Effect of process deformation history on mechanical performance of AM60B to AA6082 self-pierce riveted joints. *Eng Fract Mech* 209:92–104
22. Karim M, Jeong T, Noh W, Park K, Kam D, Kim C, Nam D, Jung H, Park Y (2020) Joint quality of self-piercing riveting (SPR) and mechanical behavior under the frictional effect of various rivet coatings. *J Manuf Process* 58:466–477
23. Hirsch F, Müller S, Machens M, Staschko R, Fuchs N, Kästner M (2017) Simulation of self-piercing rivetting processes in fibre reinforced polymers: material modelling and parameter identification. *J Mater Process Technol* 241:164–177
24. Wu CT, Wu Y, Crawford JE, Magallanes JM (2017) Three-dimensional concrete impact and penetration simulations using the smoothed particle Galerkin method. *Int J Impact Eng* 106:1–17
25. Wu CT, Bui TQ, Wu Y, Luo TL, Wang M, Liao CC, Chen PY, Lai YS (2017) Numerical and experimental validation of a particle Galerkin method for metal grinding simulation. *Comput Mech* 61:365–383
26. Huang L, Wu Y, Huff G, Huang S, Ilinich A, Freis A, Luckey G (2018) Simulation of self-piercing rivet insertion using smoothed particle galerkin method in 15th International LS-DYNA Users Conference
27. Huang L, Wu Y, Huff G, Ilinich A, Freis A, Huang S, Luckey G (2020) Sensitivity study of self-piercing rivet insertion process using smoothed particle galerkin method in 16th International LS-DYNA Users Conference
28. Wang S, Wang D (2019) Research on crashworthiness and light-weight of B-pillar based on MPSO with TOPSIS method. *J Braz Soc Mech Sci* 41:498
29. Xie C, Wang D (2020) Multi-objective cross-sectional shape and size optimization of S-rail using hybrid multi-criteria decision-making method. *Struct Multidiscip O* 62:3477–3492
30. Wang D, Xie C (2019) Contribution analysis of the cab-in-white for lightweight optimization employing a hybrid multi-criteria decision-making method under static and dynamic performance. *Eng Optimiz* 52:1903–1922
31. Ma Y, Lou M, Li Y, Lin Z (2018) Modeling and experimental validation of friction self-piercing riveted aluminum alloy to magnesium alloy. *Weld World* 62:1195–1206
32. Wu CT, Wu Y, Lyu D, Pan X, Hu W (2019) The momentum-consistent smoothed particle Galerkin (MC-SPG) method for simulating the extreme thread forming in the flow drill screw-driving process. *Computational Particle Mechanics* 7:177–191
33. Wu Y, Wu CT (2018) Simulation of impact penetration and perforation of metal targets using the smoothed particle Galerkin method. *J Eng Mech* 144:04018057
34. Song P, Li W, Wang XM (2019) A study on dynamic plastic deformation behavior of 5052 aluminum alloy. *Key Eng Mater* 812:45–52
35. Gerson M, Hein D, Gerkens M (2019) Numerical simulation of high-speed joining of sheet metal structures. *Procedia Manufacturing* 29:280–287
36. He X, Xing B, Zeng K, Gu F, Ball A (2013) Numerical and experimental investigations of self-piercing riveting. *Int J Adv Manuf Technol* 69:715–721
37. Kam D, Jeong T, Kim M, Shin J (2019) Self-piercing riveted joint of vibration-damping steel and aluminum alloy. *Appl Sci* 9:4575
38. Li D, Chrysanthou A, Patel I, Williams G (2017) Self-piercing riveting—a review. *Int J Adv Manuf Technol* 92:1777–1824

Publisher's Note Springer Nature remains neutral with regard to jurisdictional claims in published maps and institutional affiliations.